



**Environmentally friendly thermoelectric sulphide $\text{Cu}_2\text{ZnSnS}_4$
single crystals with dimensionless figure of merit ZT
achieving 1.6**

Journal:	<i>Journal of Materials Chemistry A</i>
Manuscript ID	TA-COM-04-2021-002978.R3
Article Type:	Communication
Date Submitted by the Author:	28-May-2021
Complete List of Authors:	Nagaoka, Akira; University of Miyazaki, a. Research Center for Sustainable Energy & Environmental Engineering Yoshino, Kenji; University of Miyazaki, Department of Applied Physics and Electronic Engineering Masuda, Taizo; Toyota Motor Corporation Higashifuji Research Center Sparks, Taylor; University of Utah, Materials Science and Engineering Scarpulla, Michael; University of Utah, Nishioka, Kensuke; University of Miyazaki, Research Center for Sustainable Energy & Environmental Engineering

COMMUNICATION

Environmentally friendly thermoelectric sulphide $\text{Cu}_2\text{ZnSnS}_4$ single crystals with dimensionless figure of merit ZT achieving 1.6 †

Received 00th January 20xx,
Accepted 00th January 20xx

Akira Nagaoka,^{*a} Kenji Yoshino,^b Taizo Masuda,^c Taylor D. Sparks,^d Michael A. Scarpulla^d and Kensuke Nishioka^a

DOI: 10.1039/x0xx00000x

Thermoelectrics (TEs) are an important class of technologies for harvesting electric power directly from heat sources. To design both high performance and environmentally friendly for TE materials, pseudo-cubic structure has great theoretical potential to maximize a dimensionless figure of merit ZT . TE multinary single crystal with pseudo-cubic structure paves a new path to manipulate valley degeneracy and anisotropy with low thermal conductivity caused by short-range lattice distortion. Here, we report a record high $ZT = 1.6$ around 800 K, realized in totally environmentally benign p-type Na-doped $\text{Cu}_2\text{ZnSnS}_4$ (CZTS) single crystal. The exceptional performance comes from a high power factor while maintaining intrinsically low thermal conductivity. The combination of pseudo-cubic structure and intrinsic properties in CZTS single crystal takes advantage of simple material nature tuning without complex techniques.

Introduction

Many different strategies for improving the dimensionless figure of merit $ZT = S^2\sigma T/\kappa$, where S is the Seebeck coefficient, σ is the electrical conductivity, T is temperature, and κ is the thermal conductivity, have been conducted for thermoelectric (TE) application. These concepts include, but are not limited to, phonon-glass electron-crystal¹ or phonon-liquid electron-crystal,² nanostructure modification by alloying and doping to reduce thermal conductivity or to enhance electrical properties by doping and alloying techniques,³⁻⁸ improvement of Seebeck coefficient by electronic density of states (DOS) distortion,⁹ the

conduction (valence) band tuning,¹⁰ quantum confinement effects,¹¹ and electron energy barrier filtering.¹² Low thermal conductivity is possible by inducing nanostructure^{13,14} and hierarchical architecture.^{15,16} So far, the $ZT = 2.6$ for SnSe ¹⁷ has been achieved by anisotropic properties,^{18,19} multiple valence bands,^{20,21} and three-dimensional charge and two-dimensional phonon transport.²² Nevertheless, for large-scale deployment of TE devices, TE materials will have to simultaneously fulfill tough requirements such as non-toxicity, non-scarcity and high efficiency. However, totally environmentally friendly TE materials by current strategies demonstrate far lower ZT values than TE state-of-the-art such as 1.1 for SnS .²³

Pseudo-cubic approach of multinary compounds paves a path to manipulate the electronic band structure.²⁴ The tetragonal I-III-VI₂ group chalcopyrite structure is analogous to a $1\times 1\times 2$ supercell expansion of the zinc-blende structure. It is easy for non-cubic structure to achieve low symmetry with crystal-field splitting Δ_{CF} which leads to low valley degeneracy. This approach is that Δ_{CF} could be tuned to 0 when the crystal structure parameter η is equal to 1 ($\eta = c/2a$, where c and a are lattice parameters for chalcopyrite), resulting in a pseudo-cubic structure. This long-range cubic-like structure regains the valley degeneracy and maintains the localized short-range non-cubic lattice distortions. Moreover, this study relies on the manipulation of the distortion of DOS (valley distortion) by doping technique, and the exact shape of valleys which can be expressed as the effective mass of carriers (valley anisotropy) for functional materials to accomplish application needs.

Here, the combination of pseudo-cubic structure and nature of single crystal is simply applied to achieve environmentally friendly TE material with high ZT . Single crystals are necessary for optimization of valley parameters, especially valley anisotropy. Typical TE materials have been polycrystalline because grain boundaries scatter phonons disproportionately more than they scatter electrons. This leads to a greater reduction in thermal conductivity than in electrical conductivity and therefore an overall increase in ZT in the last few decades. A pseudo-cubic approach allows the ability to

^a Research Center for Sustainable Energy & Environmental Engineering, University of Miyazaki, Miyazaki 889-2192, Japan. *E-mail: nagaoka.akira.m0@cc.miyazaki-u.ac.jp

^b Department of Applied Physics and Electronic Engineering, University of Miyazaki, Miyazaki 889-2192, Japan.

^c S-Frontier Division, Toyota Motor Corporation, Shizuoka 411-0019, Japan.

^d Department of Materials Science and Engineering, University of Utah, Salt Lake City, Utah 84112, USA.

† Footnotes relating to the title and/or authors should appear here.

Electronic Supplementary Information (ESI) available: [details of any supplementary information available should be included here]. See DOI: 10.1039/x0xx00000x

COMMUNICATION

Journal Name

simultaneously optimize electrical and thermal transport properties by long- and short-range structure regions. We focus on the quaternary I₂-II-IV-VI₄ group compound p-type Cu₂ZnSnS₄ (CZTS), which has attracted much attention, mainly in the field of photovoltaic (PV) application. The crystal structure of CZTS is kesterite, closely related to chalcopyrites. Our previous study reveals that η value of CZTS is close to 1 from neutron diffraction measurement, which is ideally suited for a pseudo-cubic approach.²⁵ High-quality large-size CZTS single crystals can be obtained to perform experimental thermoelectric measurements on bulk samples.²⁶

Results and discussion

Electronic band structure of CZTS

Fig. 1(a) depicts the ordered and disordered kesterite structures of CZTS, wherein the cation layers of Cu-Sn, Cu-Zn, Cu-Sn and Cu-Zn are alternated along the *c*-axis. In the Cu-Zn layer, the two atoms are easily disordered leading to short-range distortion for low thermal conductivity. The experimental crystal structure parameter η value of ordered kesterite CZTS is 0.997 ($a = 5.455 \text{ \AA}$ and $c = 10.880 \text{ \AA}$), which minimizes the energy splitting parameter ΔCF . The utilization of a rational pseudo-cubic structure supports cubic-like degenerate electronic bands to be high power factor (*PF*) in Fig. 1(b).

We performed the electronic band calculations of ordered and disordered kesterite structure providing its impact of TE properties in this study. The electronic band structure of ordered CZTS was computed by density functional theory (DFT) and is shown in Fig. 2(a). The spin-orbit interaction is included. Cubic-like valence band edges are observed as a result of the symmetry framework, which is highly degenerate at Γ point indicating an ideal character of pseudo-cubic structure. The band structure with direct bandgap can be observed. As is often the case, the DFT band gap is slightly smaller than the experimental value which we measured to be 1.6 eV for CZTS single crystal by using transient reflectivity measurements.²⁷ The top of the valence band is split by the crystal field for ordered and disordered CZTS in Fig. 2(b)-(c). Ordered kesterite CZTS have Γ_{7+8} symmetry for the topmost (v_1) and second (v_2) valence bands and Γ_{5+6} symmetry for the third band (v_3) where the single state is above the twofold degenerate state with $\Delta CF = -0.06 \text{ eV}$ in the vicinity of Γ point. This theoretical result is in good agreement with a pseudo-cubic approach.²⁴ We observed that Cu/Zn disorder has little impact on the electronic band structure of kesterite CZTS in Fig. 2(c) which is discussed in Supplementary Materials. The strength of the crystal field is larger in ordered structure ($\Delta CF = -0.06 \text{ eV}$) compared to the disordered structure ($\Delta CF = -0.04 \text{ eV}$). The DOS of top of the valence band, which is associated with Seebeck coefficient, for both ordered and disordered structures is shown in Fig. 2(d). The difference between both structures is little, such as slope. This result provides that disorder transition of CZTS affects the stability at high operation temperature rather than TE properties because ordered kesterite cannot exist above transition temperature. Table 1 shows the anisotropic effective hole masses of both ordered and disordered kesterite CZTS obtained directly from the band energy dispersion.

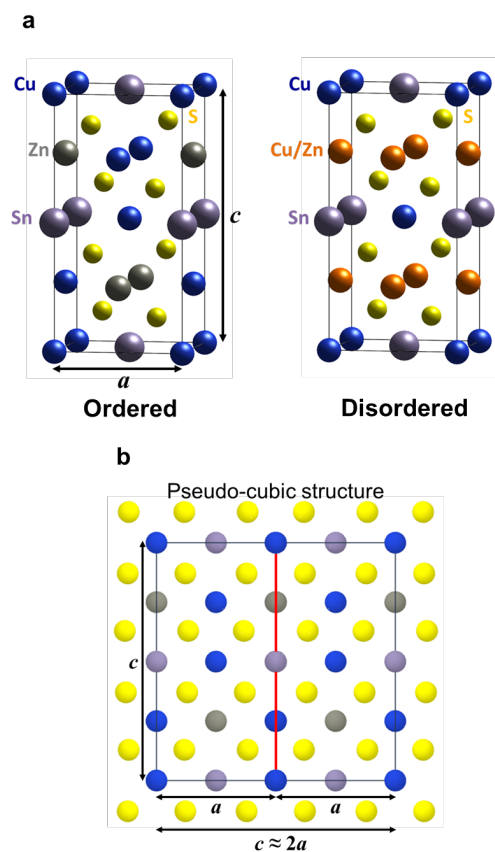


Fig. 1 Fundamental crystal structures in TE CZTS material. (a) Conventional unit cell of the ordered and disordered kesterite structures having (b) pseudo-cubic structure by the crystal structure parameter η ($c/2a \approx 1$).

Structural properties

In this study, we fabricated samples with different compositions including a stoichiometric Cu₂ZnSnS₄ (sample 1), Cu-poor Cu_{1.9}ZnSnS₄ (sample 2), Cu-poor Cu_{1.9}ZnSnS₄ with Na: 0.1 mol% doped (sample 3), and 0.04 mol% doped (sample 4) by Sn-solvent traveling heater method (THM).²⁵ Sodium is known to benefit CZTS PV devices as an effective dopant for enhancement of electrical properties.²⁸ Single crystals were cut in the transverse (\perp ; perpendicular to the *c*-axis) and the longitudinal (\parallel ; parallel to the *c*-axis) directions for thermoelectric measurements. The structural and compositional properties were investigated by powder X-ray diffraction (XRD), Raman spectroscopy, and inductively coupled plasma atomic emission spectroscopy (ICP-AES) (Fig. S1 and Table S1-S2, ESI⁺). The quality of samples 1-4 is evaluated by using X-ray rocking curve (XRC) measurement with the full width at half-maximum (FWHM) (Fig. S2, ESI⁺), which closely related with the dislocation density. The compositional homogeneity of all single crystals are less than 2 at.% throughout each ingot and wafer by energy dispersive X-ray spectroscopy (EDX) mapping

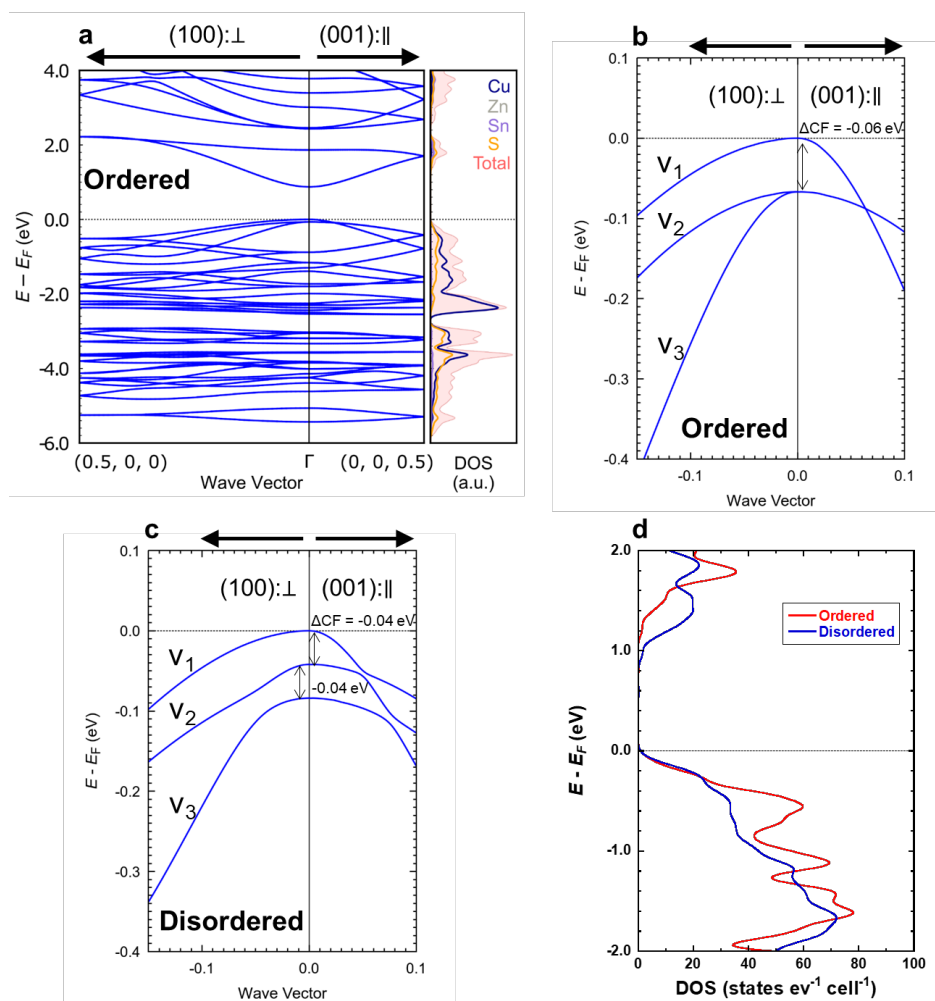


Fig. 2 Electronic band structures of ordered and disordered kesterite CZTS for pseudo-cubic based approach. (a) Electronic band structure of ordered kesterite structure of CZTS along the two symmetry directions \perp ; perpendicular to the c -axis and \parallel ; parallel to the c -axis. The top of the valence band of (b) ordered structure; and (c) disordered structure. The valence band is split into the topmost (v_1) and second (v_2) bands with Γ_{7+8} symmetry and the third band (v_3) with Γ_{5+6} symmetry where the single state is above the twofold degenerate state with the energy splitting parameter ΔCF in the vicinity of Γ point. Dashed line denotes the Fermi energy E_F . (d) The comparison of DOS for ordered and disordered CZTS.

Table 1 Anisotropy of the effective hole masses (m_n for $n = v_1, v_2,$ and v_3 in Fig. 1) in both ordered and disordered CZTS. m_e is electron mass. The transverse \perp masses are determined from the energy dispersions in (100) direction, and the longitudinal \parallel masses are determined from the dispersions in (001) direction.

	$m_{v_1}^{\perp} [m_e]$	$m_{v_1}^{\parallel} [m_e]$	$m_{v_2}^{\perp} [m_e]$	$m_{v_2}^{\parallel} [m_e]$	$m_{v_3}^{\perp} [m_e]$	$m_{v_3}^{\parallel} [m_e]$
Ordered	0.77	0.17	0.78	0.76	0.16	0.76
Disordered	0.83	0.18	0.54	0.72	0.35	0.73

measurement (Fig. S3, ESI[†]), which leads to reliable TE properties.

As mentioned, the degree of order in all kesterite CZTS samples must be determined for comprehensive study. However, disorder of Cu and Zn in kesterite structure is very difficult to determine because standard X-ray methods cannot

distinguish Cu^+ and Zn^{2+} . The Raman spectroscopy is powerful tool to assess Cu/Zn order because it reflects the symmetry of crystal structure, the strength of chemical bonds and the local atomic environment. Currently, Scragg *et al.* have suggested that the Raman peak intensity ratio of each A mode in CZTS is sensitive to the degree of order under near-resonant condition

of 785 nm laser excitation, which revealed that Cu/Zn order-disorder transition temperature was 533 K (260 °C).²⁹ Fig. 3 shows Raman spectra of stoichiometric CZTS samples for 532 nm and 785 nm excitation wavelengths. The quantitative order parameter Q was defined as intensity ratio of M_{2A}/M_{3A} , which is the second major A mode at $\sim 288\text{ cm}^{-1}$ (M_{2A}) and minor A mode at $\sim 304\text{ cm}^{-1}$ (M_{3A}) in kesterite structure. With this definition, larger value of Q means more ordered sample.²⁹ We attempted growth of stoichiometric CZTS single crystals by different cooling rate in order to investigate degree of order. The samples differed only in the cooling rate after crystal growth, which were 1–500 °C/h and quenching in water. Raman spectra of two sample with different cooling rate (20 °C/h and quenched in the water) were measured. Samples 1-4 were rapidly cooled at the rate of 500 °C/h from 700 °C after crystal growth in this study, which is much higher than critical disorder transition temperature (260 °C). Raman spectra were fitted by using a basis set of symmetrical Lorentzian peaks derived from measurements. All peaks in Fig. 3(a)-(d) correspond to reported Raman modes in kesterite structure.²⁹ Cu/Zn disorder structure results in a small peak at 332 cm^{-1} of quenched sample in 532 nm spectrum, however quantitative evaluation is difficult due to the overlapping of the dominant A mode at $\sim 339\text{ cm}^{-1}$ (M_{1A}). Both major A modes become small relative to the rest of the spectrum of 785 nm excitation, so while minor A mode, E ($\sim 368\text{ cm}^{-1}$: M_E), and B ($\sim 377\text{ cm}^{-1}$: M_B) modes have higher relative intensity. The resonant condition of 785 nm excitation makes

the spectrum sensitive to small changes in bandgap occurring because of Cu/Zn disorder, which leads to these variations.²⁹ Fig. 3(e) shows the variation in Q value for different cooling rate of stoichiometric CZTS samples, which steeply drops around 100–200 °C/h, and then approaches to quenched sample Q line. This means that very slow cooling, at least less than 100 °C/h, is required for ordered kesterite structure and we concluded that samples 1-4 were disordered kesterite structure in this study. The disordered samples are suitable for application because TE materials require to operate under temperature difference conditions. In fact, there were no change of mass until 800 K and no phase transition close to 533 K (260 °C) in disordered sample by differential scanning calorimetry (DSC) and thermogravimetric analysis (TGA) (Fig. S4, ESI†). The observation of ordered-disordered transition in CZTS single crystals is discussed by TE properties in ESI†.

TE properties

The temperature dependent electrical and TE properties of CZTS single crystals from 300 K to 800 K are shown in Fig. 4 with the accuracy of TE measurements discussed in ESI† (Fig. S5-S7). Consistent with our previous work on fundamental properties of CZTS,^{25,26,28} the electrical conductivity with a Cu-poor composition and Na-doping increased by approximately two orders of magnitude greater than the stoichiometric sample (Fig. 4(a)). We have reported that the carrier transport mechanism can be expressed by band conduction from valence band to defect level near room temperature.²⁸ The conductivity

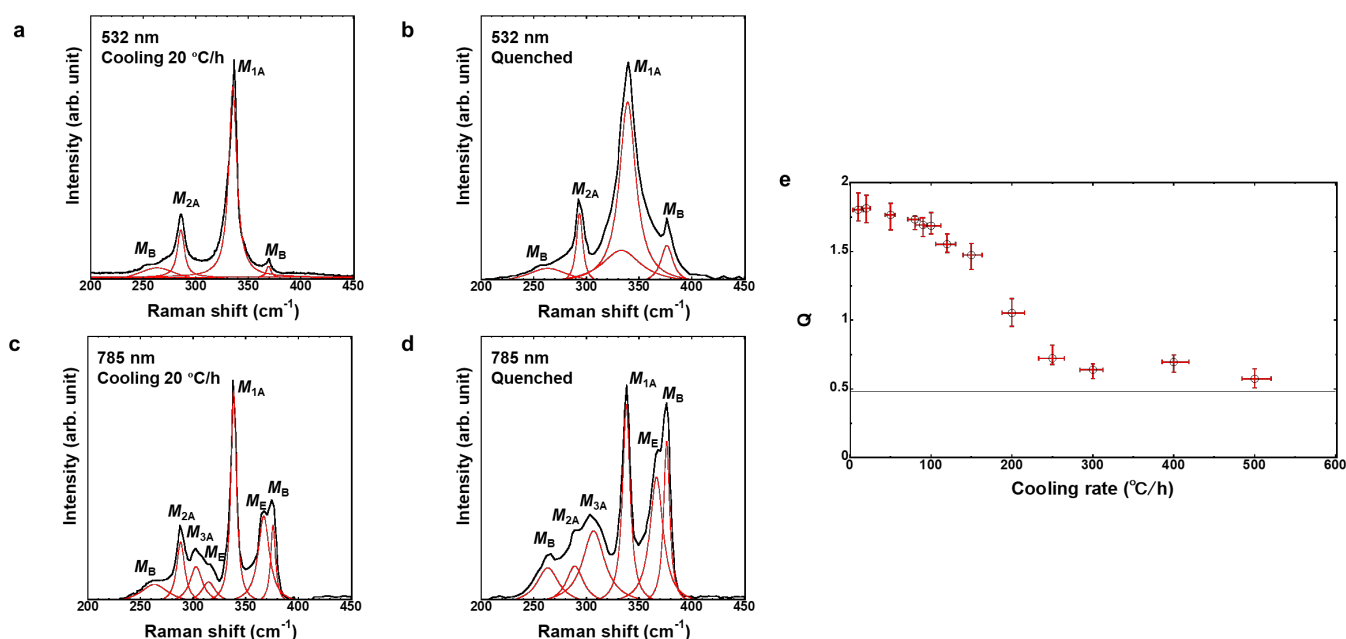


Fig. 3 Raman-based quantification for degree of order in stoichiometric CZTS (112) wafers. (a)-(d) Raman spectra for CZTS samples with different excitation wavelengths of 532 nm and 785 nm. CZTS single crystals were grown by cooling rate of 20 °C/h and quenching in water after growth process. All peaks were fitted by Lorentzian function and labeled for A, B, and E modes. (e) Variation in Q value for different cooling rate of stoichiometric CZTS samples. With Q value definition as intensity ratio of M_{2A}/M_{3A} , larger value means more ordered samples. Black line means the value of quenched sample.

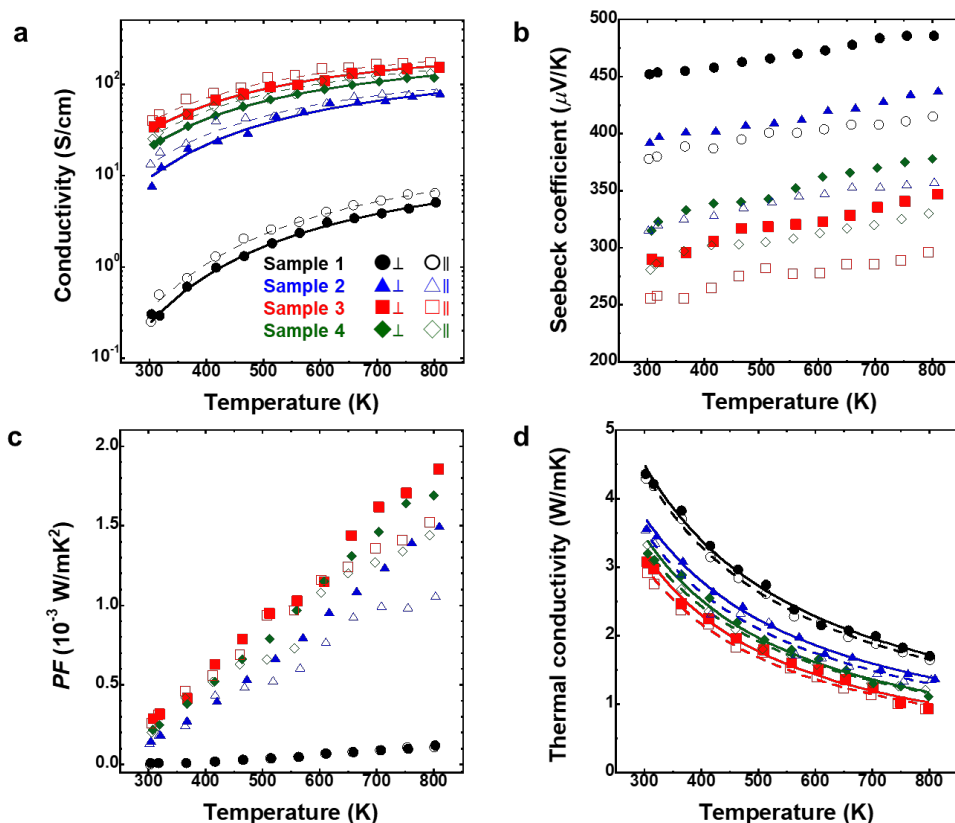


Fig. 4 TE characterization of CZTS single crystals. Temperature dependence of (a) electrical conductivity σ fitted by $\sigma(T) = \sigma_B \exp(-E_A/k_bT)$, (b) Seebeck coefficient S , (c) power factor PF , and (d) thermal conductivity κ . Lines are roughly following to a T^{-1} relation. Measurements are carried out in the transverse (\perp ; perpendicular to the c -axis) and the longitudinal (\parallel ; parallel to the c -axis) directions.

data can be described quantitatively as typical thermal activation $\sigma(T) = \sigma_B \exp\left(\frac{-E_A}{k_bT}\right)$, where σ_B is pre-factor, E_A is the relevant activation energy associated with band conduction, and k_b is the Boltzmann constant. The conduction parameters are shown in ESI† (Table S3). The Fermi level lies around the top of the valence band because of typical thermal activation. Therefore, anisotropy of topmost v_1 is dominant for electrical properties. The longitudinal m_{v1}^{\parallel} is smaller than the transverse m_{v1}^{\perp} , which leads that conductivity along c -axis is higher than that along a -axis. First-principle calculations predict that the dominant shallow V_{Cu} acceptor level under Cu-poor condition is at 20 meV above valence band maximum.³⁰ Cu on Zn antisite defect (Cu_{Zn}) becomes a dominant deep acceptor defect at 120 meV under near-stoichiometric and Cu-rich compositions.³⁰ The lower E_A in Cu-poor compositions leads to higher electrical conductivity values because of the increasing concentration of V_{Cu} acceptor. In addition, Na-doping results in the improvement of compensation by suppression of dominant Zn on Cu antisite donor defect (Zn_{Cu}).²⁸ This donor defect may be inhibited by a finite Na substitution as neutral Na substituting on Cu site (Na_{Cu}) defect, which is in good agreement with the lowest calculated formation energy of Na_{Cu} by theoretical study.³¹ Therefore, the hole mobility and concentration can be enhanced by Na-doping simultaneously in ESI† (Table S3). The scattering process is discussed from temperature dependence of hole mobility (Fig. S8, ESI†).

The sign of the Seebeck coefficient, S , is always positive for all samples as expected for these p-type materials. The values of S monotonically increase with increasing temperature because more holes are thermally activated to high energy states which leads to a higher average entropy of holes originated from valley degeneracy in Fig. 4(b). Note that S along a -axis is 10-20% higher than that of c -axis due to heavy effective hole mass from valley anisotropy. Lower S values are observed in Cu-poor compositions and with increasing Na-doping because of the enhanced hole concentration (Table S3, ESI†). So far, the reported S values of stoichiometric CZTS bulk polycrystalline samples without doping range from 260 to 990 $\mu V/K$ depending on hole concentration near 700 K.³²⁻³⁴ The temperature dependence of PF is shown in Fig. 4(c). The PF value of sample 3 along a -axis at 800 K is $1.86 \times 10^{-3} W/mK^2$, which is higher than $1.2 \times 10^{-3} W/mK^2$ of the state-of-the-art compound Cu_2Se with $ZT = 2.6$ at 850 K.³ Our result reveals that high S and σ originated by valley degeneracy and anisotropy leads to high PF value as totally environmentally TE material.

The temperature dependence of thermal conductivity, κ , is shown in Fig. 4(d), which was calculated by the thermal diffusivity, λ , specific heat capacity, C_p , and density D . The thermal diffusivity and specific heat capacity dependence on temperature are shown in ESI† (Fig. S6(b)-(c)). Weak anisotropy of thermal conductivity was observed which κ_{\perp} indicates $\sim 3\%$ larger than κ_{\parallel} . The lattice thermal conductivity along a -axis is $\sim 5\%$ larger than that of c -axis in the kesterite structure from theoretical calculation based on the phonon Boltzmann

transport.³⁵ Weak anisotropy of thermal conductivity in this study is in good agreement with theoretical study.³⁵ The thermal conductivity decreases with increasing temperature roughly according to a T^{-1} relation for all samples. This temperature dependence suggests that the lattice thermal conductivity is primarily driven by phonon-phonon Umklapp scattering rather than intrinsic defects. If phonon scattering were driven by neutral dopant-induced, anti-site disorder, or alloy scattering then the scattering would be more uniform over the temperature range with very weak temperature dependence. Such thermal conductivity temperature dependence is typically observed in heavily defected materials such as yttria-stabilized zirconia.³⁶ However, here the T^{-1} temperature dependence characteristic of phonon-phonon scattering occurs when other mechanisms like neutral defect scattering are less important. In fact, literature examples exist where the thermal conductivity trend transitions from T^{-1} to nearly temperature independent due to anti-site disorder or mixtures of point defects with Umklapp scattering.^{37,38} In this work, we see evidence that lattice scattering is impacted by the intrinsic complexity of the crystallographic structure. For example, consider the disorder between Cu and Zn by off-stoichiometric compositions and Na-doping. Even though these are single crystals which do not benefit from lattice thermal conductivity reduction due to grain boundary scattering, the values of κ at 800 K are only between 0.94 to 1.7 W/mK. Such low values are only moderately higher than the other reported values of related polycrystalline quaternary compounds such as CZTSe and $\text{Cu}_2\text{CdSnSe}_4$.^{39,40} We focused on the other factor of low thermal conductivity in CZTS by potential for lattice anharmonicity as the Grüneisen parameter. Currently, theoretical calculations demonstrate that TE materials with low thermal conductivity have large Grüneisen parameter such as 2.1 along b -axis for SnSe,¹⁷ 2.05 for AgSbTe₂⁴¹ and 3.5 for AgSbSe₂.⁴² In fact, the Grüneisen parameter value of 2.28 for CZTS was reported by DFT calculation,⁴³ which is likely to lead to intrinsically low thermal conductivity in this study even though there are some factors for lattice thermal conductivity and lattice anharmonicity such as phonon mean free path and the elastic properties.

The ability to achieve such low thermal conductivity due to the intrinsic defects in this material while maintaining good electrical transport is an unexpected improvement which can be attributed to the single crystal nature of these samples. Grain boundaries are typically known to present energy barriers of order 50-150 meV in polycrystalline chalcogenide semiconductors like CZTS.⁴⁴ Recent literature points out that continued ZT enhancement due to lattice thermal conductivity reduction is fundamentally limited without a means whereby the PF is also enhanced.⁴⁵ In light of this, the single crystal approach with a site-disordered material is promising.

Taken together, the outstanding electrical properties with relatively low thermal conductivity of sample 3 resulted a totally environmentally friendly TE material with TE figure of merit up to $ZT = 1.6$ at 800 K (Fig. 5). This value is comparable to the highest ZT reported for other relating quaternary polycrystalline materials because the PF value of $1.86 \times 10^{-3} \text{ W/mK}^2$ in this study is 2-15 times larger than those in literatures (Table S5, ESI[†]). The combined uncertainty of all measurements involved in the calculation of ZT leads to an estimated uncertainty near 30%. Our approach is comparable with phonon-liquid electron-

crystal concept discovering non-toxic earth-abundant Cu_{2-x}S with $ZT = 1.7$ at 1000 K.⁴⁶

Enhancement of electrical and TE properties

Admittance spectroscopy (AS) measurements were used to characterize the defect levels and concentrations in samples. Fig. 6(a) shows an Arrhenius plot to verify the defect levels, which were extracted from inflection points from the AS curves in Fig. 6(b)-(d). All parameters for AS measurement are shown in ESI[†] (Table S3). The activation energy, $E(\omega)$, were obtained from the slope of the Arrhenius plot, $\ln(\omega_0/T^2)$ versus $1/T$, where ω_0 is the inflection point of the capacitance versus frequency. The shallow acceptor level becomes lower in the Cu-poor composition from 100 meV to 65 meV because the dominant acceptor is V_{Cu} . The Na-doping in Cu-deficient compositions results in two orders of magnitude higher hole concentration compared to stoichiometric compositions because there is a reduction in the degree of compensation.²⁸ The dual advantages of lower thermal activation energy and higher hole concentration dramatically improve electrical properties by tuning composition and doping.

The Seebeck coefficient of CZTS single crystal along a -axis is large, for example as Na: 0.1 mol% sample 3, 290 $\mu\text{V/K}$ at 300 K and 347 $\mu\text{V/K}$ at 800 K. As mentioned above, we suggested that it is possible to tune DOS by the formation of V_{Cu} in Cu-deficient samples and Na-doping. The energetic defect DOS is obtained by converting frequency into energy by using equations (1) and (2),⁴⁷

$$E(\omega) = k_{\text{B}}T \cdot \ln\left(\frac{2\xi T^2}{\omega}\right) \quad (1)$$

$$N_{\text{t}}(E(\omega)) = -\frac{V_{\text{bi}}}{W_{\text{d}}} \cdot \frac{dC}{d\omega} \cdot \frac{\omega}{k_{\text{B}}T} \quad (2)$$

where N_{t} is integrated defect density, ξ is pre-exponential factor comprising all temperature independent terms, V_{bi} is built-in potential, W_{d} is depletion width. V_{bi} and W_{d} are

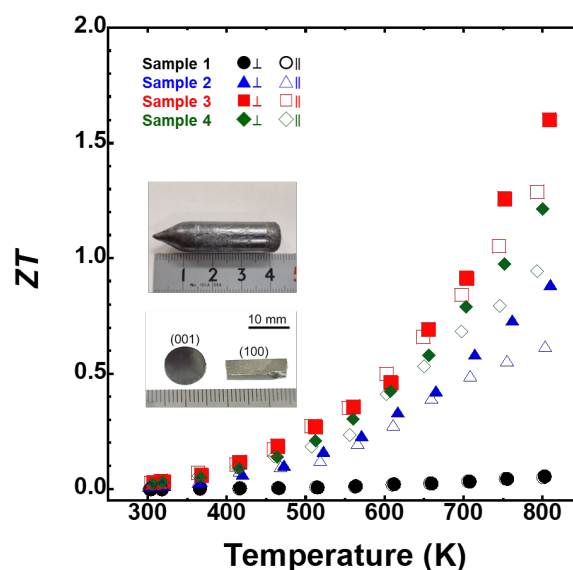


Fig. 5 Temperature dependence of the dimensionless figure of merit ZT for different compositional CZTS single crystals. The insets are a typical CZTS ingot and samples cutting along the (100) and (001) planes.

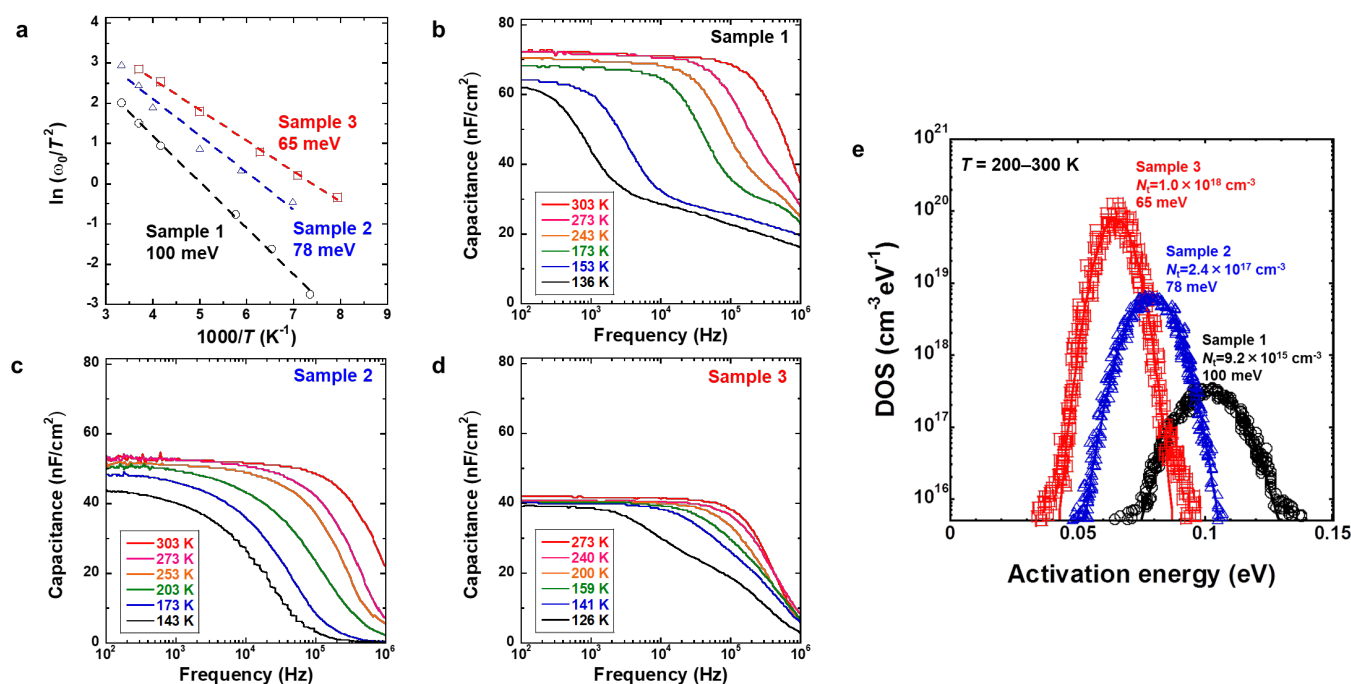


Fig. 6 The defect level and DOS of CZTS single crystals extracted by AS measurement as a function of temperature. (a) Arrhenius plot of $\ln(\omega_0/T^2)$, ω_0 being the angular emission frequency of the inflection points. (b)-(d) Temperature dependence of AS spectra of each sample. (e) N_t calculated from AS measurement for different compositional samples. The defect level and DOS values are shallower and higher with Cu-poor and Na-doping, respectively. Associated integrated N_t is calculated based on Gaussian fitting. No anisotropy of defect properties can be observed.

extracted from capacitance-voltage measurement (Fig. S10, ESI[†]). Fig. 6(e) reveals DOS of dominant acceptor levels extracted from AS data. The enhancement of DOS with shallow acceptor and Na-doping relating to TE properties can be observed. The acceptor concentration in CZTS single crystals is higher than that of CZTS-based PV absorber layer extracted from AS data.⁴⁸ There are some factors relating to defect concentration, such as the composition, grain-boundary, and growth condition in CZTS. This is likely associated with low defect compensation in high-quality single crystal sample.²⁸ Our results will be a good reference for future work to investigate the defect properties. Considering the impact of Na on DOS in CZTS, perhaps low compensation, we present the DOS for the Na-dopant substitution on Cu by DFT calculation (Fig. S12, ESI[†]). There is no significant increase in DOS by Na_{Cu} defect, on the other hand the effective masses for each valence band are slightly larger than stoichiometric CZTS (Table S6, ESI[†]). Other possible Na impact on DOS is the increasing of Na substitution on Zn site (Na_{Zn}) shallow acceptor defect which is low formation energy next to Na_{Cu} .³¹ We experimentally demonstrate that DOS in CZTS can be improved by Cu-deficit and Na-doping for high TE performance.

Conclusions

In this study, our focus was to first achieve competitive ZT values for kesterite CZTS as totally environmentally friendly TE material by pseudo-cubic approach with disordered structure. The value of $ZT = 1.6$ at 800 K in high-quality p-type CZTS single

crystals is remarkable and due primarily to high degeneracy at valence band edge (valley degeneracy), the anisotropy of effective mass (valley anisotropy) and localized lattice distortion. Several insights (i)-(iii) for a high ZT quaternary compound can be highlighted from this study as follows: (i) high PF value $1.9 \times 10^{-3} \text{ W/mK}^2$ at 800 K was obtained by tuning valley parameters, (ii) the intrinsic local cation anti-site disorder and compositional domain results in a low thermal conductivity of $\sim 0.94 \text{ W/mK}$ at 800 K even for single crystal samples, (iii) Cu-deficient composition and Na-doping lead to high electrical and TE properties due to V_{Cu} and Na related shallow acceptor defects. Compared to other high performance TE materials, our results for CZTS demonstrate that a high ZT can be realized in an intrinsic structure, as single crystal, with simple tuning by composition and doping without complex nanostructuring. Our approach based on multinary compound single crystal have a potential to produce intrinsic TE material compared with state-of-the-art concepts. We expect the discovery of high TE performance for CZTS could attract great attention within the waste heat recovery industry due to the totally environmentally friendly combination of elements that are low cost, non-toxic, and earth-abundant.

The ZT curve in this study approximately displays an exponential increase with temperature, which indicates the average ZT in the studied temperature range is still low. The state-of-the-art TE materials, such as Cu_2Se ,³ SnSe ,¹⁷ and Cu_{2-x}S ,⁴⁶ demonstrated similar exponential ZT curve when they were firstly reported. So far, ZT properties for these materials have

been improved by various techniques, which is our ongoing study for TE CZTS.

Experimental detail

Single crystal growth

CZTS single crystals were grown by Sn-solvent traveling heater method (THM) at 40 °C/cm axial temperature gradient, a growth temperature at 850 °C, at a growth speed of 4 mm/day. The details are explained in ESI†. A conical quartz ampoule was coated with carbon to avoid solution adhesion. The detailed composition of the crystals was determined by inductively coupled plasma atomic emission spectroscopy (ICP-AES; SII NanoTechnology SPS3520UV). Samples were dissolved into a mixed acid containing HNO₃ and HCl.

Sample preparation before characterization

Grown crystals were cut with a diamond blade and polished mechanically with 0.01 μm Al₂O₃ powder and then etched with a HCl solution for 5 minutes to remove saw and polishing damage. The electrical and TE measurements were carried out along the *c*-axis (Fig. S1(c), ESI†).

DFT calculation

First-principle calculations were performed using the plane-wave basis projector augmented wave (PAW)⁴⁹ method and the generalized gradient approximation (GGA) of Perdew-Burke-Ernzerhof (PBE)⁵⁰ implemented in Vienna *Ab initio* Simulation Package (VASP).^{51,52} The planewave basis-set cutoff was set to 300 eV and spin polarization was considered. We used the PAW potentials which treat Cu (3d¹⁰ 4s¹), Zn (3d¹⁰ 4s²), Sn (4d¹⁰ 5s² 5p²), S (3s² 3p⁴), and Na (2p⁶ 3s¹) explicitly as valence electrons and the rest as core electrons. We adopted the effective Hubbard *U* values of 5.2 eV for Cu, 6.5 eV for Zn, and 3.5 eV for Sn. Atomic positions and the unit cell parameters were relaxed until the forces on all atoms become less than 2.0×10⁻² eV/Å. The disordered and Na-doped models were calculated within a 2×2×1 supercell of the conventional unit cell (Fig. S11, ESI†). A Na-doped model with the concentration of 6.25% was constructed by substituting a Na atom for a Cu site. The substitution for Cu 2a site was considered because the energy was lower than that for Cu 2c site. The Brillouin zones were sampled with 4×4×2 and 2×2×2 Monkhorst–Pack *k*-point meshes for the unit cell and 2×2×1 supercell, respectively. For electronic DOS, the 2×2×1 supercell and finer Γ -centered *k*-point mesh of 4×4×4 were used for pristine, disordered, and Na-doped CZTS models. For electronic band structure, a conventional unit cell instead of a primitive cell was intentionally used for the ease of analyzing anisotropic effective masses along the *a* and *c* directions. The band unfolding for the disordered and Na-doped supercell were performed using Band UP code.⁵³

Characterization

The structural properties were analyzed by powder X-ray diffraction (XRD; Panalytical X'Pert PRO) and Raman spectroscopy (HORIBA T64000). XRD measurement was operated under 40 kV and 40 mA using a Cu-K α radiation

source. The 532 nm and 785 nm laser excitation sources were used in the Raman measurements and focused on the sample by an objective lens with a numerical aperture of 0.55. The laser power on the sample was 100 mW. The spectra were calibrated based on 520 cm⁻¹ of Si peak. The orientation and crystallinity of CZTS single crystals were investigated by X-ray rocking curve (XRC; Panalytical X'Pert PRO). XRC measurement was operated under 45 kV and 40 mA with step width 0.002° using a Cu-K α radiation source.

A scanning electron microscope (SEM; Hitachi S-5500) equipped with EDX was used for compositional measurements. The conventional ZAF (atomic number, absorption, and fluorescence) corrections were performed for EDX.

The electrical conductivity σ and Seebeck coefficient *S* were measured simultaneously in a helium atmosphere at 300–800 K using a commercial system (ZEM3; ADVANCE RIKO) on the samples with the dimension of about 2 mm×2 mm×10 mm. Thermal conductivity κ was calculated based on the equation: $\kappa = \lambda C_p D$, where λ is the thermal diffusivity, C_p is the specific heat capacity, and *D* is the density. The thermal diffusivity was measured by laser flash method (Netzsch; LFA457) on the rectangular samples with 8 mm×8 mm×1 mm coated with a thin layer of graphite to minimize errors from the emissivity of the material. The specific heat capacity was measured by differential scanning calorimetry (DSC; Rigaku Thermo plus EVO2 DSCvesta) on the samples with 3 mm×3 mm×3 mm. The mass of all samples is unchanged after measurements by using Thermogravimetric analysis (TGA) (Fig. S9, ESI†). The density values between 4.4–4.5 g/cm³ were measured using the Archimedes method at room temperature.

The hole concentration *p* and mobility μ were measured by temperature dependence of Hall effect (TOYO; ResiTest8300) performed in a 0.45 T magnetic field in the van der Pauw geometry under a helium atmosphere at 20–800 K. For Hall measurements, Au contacts, each with a diameter of 1 mm and thickness of 200–300 nm, were evaporated onto the corners of each CZTS bulk single crystal with the dimension of 5 mm×5 mm×0.8 mm.

Admittance spectroscopy measurements were carried out in the temperature of 120–300 K under dark condition with a LCR meter (HP 4284A), which applied an AC voltage of 50 mV by varying the frequencies from 100 Hz to 1 MHz. Schottky diode structures of 1 mm diameter Al Schottky contact/CZTS (5 mm×5 mm×1 mm)/Au Ohmic back contact were fabricated by evaporation. The thickness of contacts was 300–400 nm.

Author contributions

A.N. and K.N. designed, conducted the all experiments and prepared the manuscript. K.Y. and M.A.S helped in single crystal growth and electrical measurements. T.M. conducted theoretical calculation. T.D.S. helped in thermoelectric measurements. All authors contributed to the discussion of results and approved the final version of the manuscript.

Conflicts of interest

There are no conflicts to declare.

Author contributions

This work was supported by the JSPS KAKENHI Grant Number JP20K15221. A.N. was supported by 2020 Young Researcher Award from Kenjiro Takayanagi Foundation. T.D.S. was supported by National Science Foundation CAREER award 1651668.

References

- G. A. Slack, *New Materials and Performance Limits for Thermoelectric Cooling in CRC Handbook of Thermoelectrics*, CRC Press, 1995.
- H. Liu, X. Shi, F. Xu, L. Zhang, W. Zhang, L. Chen, Q. Li, C. Uher, T. Day and G. J. Snyder, *Nat. Mater.*, 2012, **11**, 422-425.
- A. A. Olvera, N. A. Moroz, P. Sahoo, P. Ren, T. P. Bailey, A. A. Page, C. Uher and P. F. P. Poudeu, *Energy Environ. Sci.*, 2017, **10**, 1668-1676.
- M. Ibáñez, Z. Luo, A. Genç, L. Piveteau, S. Ortega, D. Cadavid, O. Dobrozhan, Y. Liu, M. Nachttegaal, M. Zebarjadi, J. Arbiol, M. V. Kovalenko and A. Cabot, *Nat. Commun.*, 2016, **7**, 10766.
- J. Zhang, L. Song, S. H. Pedersen, H. Yin, L. T. Hung and B. B. Iversen, *Nat. Commun.*, 2017 **8**, 13901.
- Y. Luo, J. Yang, Q. J. Jiang, W. Li, D. Zhang, Z. Zhou, Y. Cheng, Y. Ren and X. He, *Adv. Energy Mater.*, 2016, **6**, 1600007.
- C. Fu, S. Bai, Y. Liu, Y. Tang, L. Chen, X. Zhao and T. Zhu, *Nat. Commun.*, 2015, **6**, 8144.
- Y. Cheng, J. Yang, Q. Jiang, D. He, J. He, Y. Luo, D. Zhang, Z. Zhou, Y. Ren and J. Xin, *J. Mater. Chem., A*, 2017, **5**, 5163-5170.
- J. P. Heremans, V. Jovovic, E. S. Toberer, A. Saramat, K. Kurosaki, A. Charoenphakdee, S. Yamanaka and G. J. Snyder, *Science*, 2008, **321**, 554-557.
- H. Wang, Z. M. Gibbs, Y. Takagiwa and G. J. Snyder, *Energy Environ. Sci.*, 2014, **7**, 804-811.
- L. D. Hicks and M. S. Dresselhaus, *Phys. Rev. B*, 1993, **47**, 12727-12731.
- J. P. Heremans, C. M. Thrush and D. T. Morelli, *Phys. Rev. B*, 2004, **70**, 115334.
- K. F. Hsu, S. Loo, F. Guo, W. Chen, J. S. Dyck, C. Uher, T. Hogan, E. K. Polychroniadis and M. G. Kanatzidis, *Science*, 2004, **303**, 818-821.
- K. Biswas, J. He, Q. Zhang, G. Wang, C. Uher, V. P. Dravid and M. G. Kanatzidis, *Nat. Chem.*, 2011, **3**, 160-166.
- K. Biswas, J. He, I. D. Blum, C. I. Wu, T. P. Hogan, D. N. Seidman, V. P. Dravid and M. G. Kanatzidis, *Nature*, 2012, **489**, 414-418.
- X. Su, P. Wei, H. Li, W. Liu, Y. Yan, P. Li, C. Su, C. Xie, W. Zhao, P. Zhai, Q. Zhang, X. Tang and C. Uher, *Adv. Mater.*, 2017, **29**, 1602013.
- L. D. Zhao, S. H. Lo, Y. Zhang, H. Sun, G. Tan, C. Uher, C. Wolverton, V. P. Dravid and M. G. Kanatzidis, *Nature*, 2014, **508**, 373-377.
- C. W. Li, J. Hong, A. F. May, D. Bansal, S. Chi, T. Hong, G. Ehlers and O. Delaire, *Nat. Phys.*, 2015, **11**, 1063-1069.
- A. T. Duong, V. Q. Nguyen, G. Duvjir, V. T. Duong, S. Kwon, J. Y. Song, J. K. Lee, J. E. Lee, S. Park, T. Min, J. Lee, J. Kim and S. Cho, *Nat. Commun.*, 2016, **7**, 13713.
- L. D. Zhao, G. Tan, S. Hao, J. He, Y. Pei, H. Chi, H. Wang, S. Gong, H. Xu, V. P. Dravid, C. Uher, G. J. Snyder, C. Wolverton and M. G. Kanatzidis, *Science*, 2016, **351**, 141-144.
- K. Peng, X. Lu, H. Zhan, S. Hui, X. Tang, G. Wang, J. Dai, C. Uher, G. Wang and X. Zhou, *Energy Environ. Sci.*, 2016, **9**, 454-460.
- C. Chang, M. Wu, D. He, Y. Pei, C. F. Wu, X. Wu, H. Yu, F. Zhu, K. Wang, Y. Chen, L. Huang, J. F. Li, J. He and L. D. Zhao, *Science*, 2018, **360**, 778-783.
- H. Wu, X. Lu, G. Wang, K. Peng, H. Chi, B. Zhang, Y. Chen, C. Li, Y. Yan, L. Guo, C. Uher, X. Zhou and X. Han, *Adv. Energy Mater.*, 2018, **8**, 1800087.
- J. Zhang, R. Liu, N. Cheng, Y. Zhang, J. Yang, C. Uher, X. Shi, L. Chen and W. Zhang, *Adv. Mater.*, 2014, **26**, 3848-3853.
- A. Nagaoka, K. Yoshino, H. Taniguchi, T. Taniyama and H. Miyake, *J. Crystal Growth*, 2012, **341**, 38-41.
- A. Nagaoka, T. Masuda, S. Yasui, T. Taniyama and Y. Nose, *Appl. Phys. Express*, 2018, **11**, 051203.
- L. Q. Phuong, M. Okano, G. Yamashita, M. Nagai, M. Ashida, A. Nagaoka, K. Yoshino and Y. Kanemitsu, *Phys. Rev. B*, 2015, **92**, 115204.
- A. Nagaoka, H. Miyake, T. Taniyama, K. Kakimoto, Y. Nose, M. A. Scarpulla and K. Yoshino, *Appl. Phys. Lett.*, 2014, **104**, 152101.
- J. J. S. Scragg, L. Choubrac, A. Lafond, T. Ericson and C. Platzer-Björkman, *Appl. Phys. Lett.*, 2014, **104**, 041911.
- S. Chen, J. -H. Yang, X. G. Gong, A. Walsh and S. -H. Wei, *Phys. Rev. B*, 2010, **81**, 245204.
- W. Xiao, J. N. Wang, X. S. Zhao, J. W. Wang, G. J. Huang, L. Cheng, L. J. Jiang and L. G. Wang, *Solar Energy*, 2015, **116**, 125-132.
- M. L. Liu, F. Q. Huang, L. D. Chen and I. W. Chen, *Appl. Phys. Lett.*, 2009, **94**, 202103.
- H. Yang, L. A. Jauregui, G. Zhang, Y. P. Chen and Y. Wu, *Nano Lett.*, 2012, **12**, 540-545.
- A. Kosuga, M. Matsuzawa, A. Horie, T. Omoto and R. Funahashi, *Jpn. J. Appl. Phys.*, 2015, **54**, 061801.
- T. Gürel, C. Sevik and T. Çağın, *Phys. Rev. B*, 2011, **84**, 205201.
- D. R. Clarke and S. R. Phillpot, *materialstoday*, 2005, **8**, 22-29.
- T. D. Sparks, P. A. Fuierer and D. R. Clarke, *J. Am. Ceram. Soc.*, 2010, **93**, 1136-1141.
- Z. Qu, T. D. Sparks, W. Pan and D. R. Clarke, *Acta Materialia*, 2011, **59**, 3841-3850.
- X. Y. Shi, F. Q. Huang, M. L. Liu and L. D. Chen, *Appl. Phys. Lett.*, 2009, **94**, 122103.
- M. Ibáñez, D. Cadavid, R. Zamani, N. G. -Castelló, V. I. -Roca, W. Li, A. Fairbrother, J. D. Prades, A. Shavel, J. Arbiol, A. P. -Rodríguez, J. R. Morante and A. Cabot, *Chem. Mater.*, 2012, **24**, 562-570.
- D. T. Morelli, V. Jovovic and J. P. Heremans, *Phys. Rev. Lett.*, 2008, **101**, 035901.
- M. D. Nielsen, V. Ozolins and J. P. Heremans, *Energy Environ. Sci.*, 2013, **6**, 570-578.
- X. He and H. Shen, *Physica B*, 2011, **406**, 4604-4607.
- V. Kosyak, M. A. Karmakar and M. A. Scarpulla, *Appl. Phys. Lett.*, 2012, **100**, 263903.
- M. W. Gaultois and T. D. Sparks, *Appl. Phys. Lett.*, 2014, **104**, 113906.
- Y. He, T. Day, T. Zhang, H. Liu, X. Shi, L. Chen and G. J. Snyder, *Adv. Mater.*, 2014, **26**, 3974-3978.
- T. Walter, R. Herberholz, C. Müller and H. W. Schock, *J. Appl. Phys.*, 1996, **80**, 4411-4420.
- D. B. Khadka, S. Kim and J. Kim, *J. Phys. Chem. C*, 2015, **119**, 12226-12235.
- P. E. Blöchl, *Phys. Rev. B*, 1994, **50**, 17953-17979.
- J. P. Perdew, K. Burke and M. Ernzerhof, *Phys. Rev. Lett.*, 1996, **77**, 3865-3868.
- G. Kresse and J. Hafner, *Phys. Rev. B*, 1993, **47**, 558-561.
- G. Kresse and J. Furthmüller, *Phys. Rev. B*, 1996, **54**, 11169-11186.
- P. V. C. Medeiros, S. Stafström and J. Björk, *Phys. Rev. B*, 2014, **89**, 041407(R).